Contributed paper

OPTO-ELECTRONICS REVIEW 7(4), 347–356 (1999)

Numerical simulations for HgCdTe related detectors

S.D. YOO[1*], N.H. JO[3], B.G. KO[2], J. CHANG[2], J.G. PARK[1], and K.D. KWACK[2]

[1]Advanced Semiconductor Material and Device Development Centre, Hanyang University Seoul 133-791, Korea

[2]Department of Electronic Engineering, Hanyang University, Seoul 133-791, Korea

[3]Hyundai Electronics Industries Co., Ichon 467-701, Korea

In this paper we introduce a new HgCdTe 2-dimensional numerical simulator, HanYang University Semiconductor Device Simulator (HYSEDES). HYSEDES adopts the modified transport models to describe the inherent natures of HgCdTe such as the degeneracy, the nonparabolic conduction band, and the band offset at heterointerface. It also takes into account various generation-recombination mechanisms regarding tunnelling phenomena and optical generation. For the advanced devices employing multiple junctions, all the material parameters are described as a function of the position. The simulation results are reported for photovoltaic devices and focal plane array. We also proposed a structure to improve the characteristics in focal plane array, i.e., to reduce crosstalk with slight degrading quantum efficiency.

Keywords: HgCdTe, 2D numerical simulator, photovoltaic devices, FPA.

1. Introduction

As the realisation of the HgCdTe devices is complicate and spends time and cost, the device simulation has become a critical tool for developing the devices. In order to improve the device performance and to widen the application area, various device structures have been proposed [1,2]. The demand for accurate HgCdTe device simulator, then, is increasing. The analysis of characteristics for the HgCdTe devices has relied mostly on analytic models. The commercial simulators [3] don't fully account the degeneracy, the nonparabolic conduction band, and the band-offset on hetero-interface, and their effects on the operation characteristics.

When the degeneracy and nonparabolic effects are omitted, there could be enormous errors in the calculation of electron concentration [4], which causes an overestimated dark current in the device. It could be seen likely that considerable amount of the current flows even at zero-bias under the dark-state. Most workers have overlooked the nonparabolic effect on the current calculation. None has tried to find out the cause of the large current [3]. Another problem in the simulators is that various tunnelling processes are not included [5,6]. Regarding the various generation-recombination mechanisms including tunnelling is an essential part in clarifying the origin of the abnormal current. The suitable models, however, have not been set on the simulators yet. Consequently, to resolve these two crucial problems, proper numerical models and methods are required. We have concentrated on developing a new simulator for HgCdTe devices, HanYang University Semiconductor Device Simulator (HYSEDES).

As the process technology is greatly advanced, the high density of the detectors can be achieved. Then, the crosstalk causing image spreading becomes one of the obstacles in further integration. There are some techniques to reduce crosstalk; gettering, trench, guard ring, antireflection coating. Unfortunately, improving the crosstalk characteristic results in deterioration of quantum efficiency. High quantum efficiency is required for image processing and sensitivity.

In the first part of this paper, we will describe the modified models to solve the problems in the conventional simulators. In the second part, the numerical methods used in HYSEDES will be presented briefly.

*e-mail: sangdy@shira.hanyang.ac.kr

2. Simulation model

2.1. Transport equations

The basic semiconductor equations [7,8] to analyse the devices including heterostructure devices are given by

$$\overline{\nabla} \bullet \varepsilon \overline{\nabla}(\psi - \theta) = -q(p - n + N_D^+ - N_A^-) - \rho_S, \quad (1)$$

$$\frac{\partial n}{\partial t} = \frac{1}{q}\nabla \bullet \vec{J}_n + G_n - R_n, \quad (2)$$

$$\frac{\partial p}{\partial t} = -\frac{1}{q}\nabla \bullet \vec{J}_p + G_n - R_n, \quad (3)$$

$$\vec{J}_n = -q\mu_n n\vec{\nabla}\Phi_n, \quad \vec{J}_n = -q\mu_p p\vec{\nabla}\Phi_p, \quad (4)$$

where θ is the band structure parameter given by

$$\theta = \frac{E_g}{2q} + \frac{kT}{2q}\ln\left(\frac{N_c}{N_v}\right) + \chi, \quad (5)$$

where χ is the electron affinity and E_g is the band gap energy. N_c and N_v are the effective density of states of the conduction and of the valence band, respectively. J_n and J_p represent the electron and hole current densities. ε is the dielectric constant of the material, and ψ is the electrostatic potential defined as the intrinsic Fermi potential. q, p, n, N_D^+, and N_A^- are the electron charge, hole concentration, electron concentration, ionised donor concentration, and ionised acceptor concentration, respectively. μ_n and μ_p denote electron and hole mobilities. Φ_n and Φ_p are the quasi-Fermi potentials for the electron and hole. Along with the basic equations, precise representation for the carrier concentration is needed as well. Figure 1 shows the reduced Fermi energy referencing the conduction band edge energy, E_c, and carrier concentration as a function of the donor density. In the figure, the lines labelled 1 are for the using Boltzmann statistics, 2 for the Fermi-Dirac statistics, 3 for the Fermi-Dirac with the nonparabolic effect, and the symbol • for the Laguerre formula [9]. As the doping density increases, the band becomes degenerate, which leads $|pn - n_i^2|$ to deviate largely from zero. It indicates that the nonparabolic band and degeneracy have a great role on the carrier concentration. Even though this is well known property, it is worth to note that the deviation of $|pn - n_i^2|$ causes the simulation error. For example, a large current can be obtained even at zero-bias without illumination. Thus, in order to take into account the degeneracy effect properly, the precise model for the carrier concentration especially for the intrinsic carrier concentration is required.

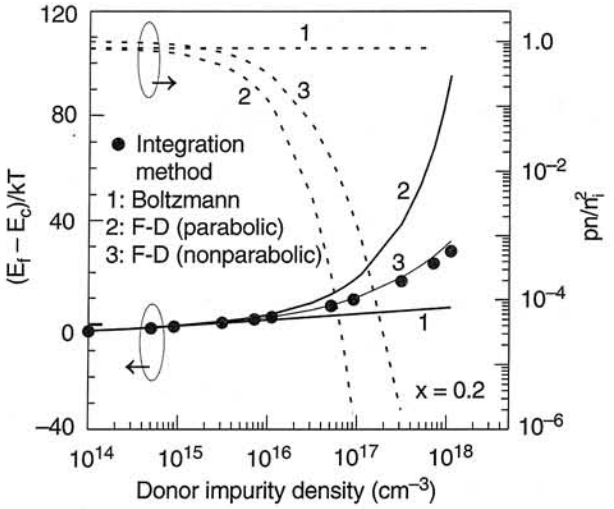

Fig. 1. The reduced Fermi energy of $(E_f - E_c)/kT$ and pn/n_i^2 as a function of donor density.

A conventional formula for the electron concentration considering the nonparabolicity and degeneracy is given by [10]

$$n = N_c\left\{F_{1/2}\left(\frac{E_{fn} - E_c}{kT}\right) + 3.75\alpha F_{3/2}\left(\frac{E_{fn} - E_n}{kT}\right)\right\}, \quad (6)$$

where the function F represents the Fermi-Dirac integral, E_{fn} is the electron quasi-Fermi level, and α is the nonparabolic factor [11]. With the equation (6) it is difficult to discretise the continuity equations using the Scharfetter-Gummel method. The following Boltzmann type formula is rather used [12]

$$n = n_i\gamma_n \exp\left(\frac{\psi - \Phi_n}{kT/q}\right), \quad (7)$$

$$\gamma_n = \frac{F_{1/2}(\eta_c) + 3.75\alpha F_{2/3}(\eta_c)}{(1 + 3.75\alpha)\exp(\eta_c)}, \quad (8)$$

where η_c is reduced electron quasi-Fermi energy, $(E_{fn} - E_c)/kT$, and n_i is the intrinsic carrier concentration. Because the valence band can be treated as parabolic band, the hole concentration is defined by

$$p = n_i\gamma_p \exp\left(\frac{\Phi_p - \psi}{kT/q}\right), \quad (9)$$

$$\gamma_p = \frac{F_{1/2}(\eta_v)}{\exp(\eta_v)}, \qquad (10)$$

where η_v is reduced hole quasi-Fermi energy, $(E_c - E_{fp})/kT$. Therefore, regarding the nonparabolicity and degeneracy, the effective intrinsic carrier concentration becomes

$$n_{ic}^2 = N_c N_v \gamma_n \gamma_p \exp(-E_g/kT) = n_i^2 \gamma_n \gamma_p. \qquad (11)$$

Rearranging Eqs. (7) and (9) in terms of the Φ_n and Φ_p, the electron and hole current equations become

$$\vec{J}_n = kT\mu_n \nabla_n + q\mu_n n\left[-\nabla\left(\psi + \frac{kT}{q}\ln(n_i\gamma_n)\right)\right], \qquad (12)$$

$$\vec{J}_p = -kT\mu_p \nabla_p + q\mu_p p\left[-\nabla\left(\psi + \frac{kT}{q}\ln(n_i\gamma_p)\right)\right]. \qquad (13)$$

The electron affinity rule model [13] for III–V compounds and the common anion rule model [14] for HgCdTe have been used for band-offset at hetero-interface. In addition, the band parameter θ should be modified according to the nonparabolicity and the band-offset

$$\theta = \frac{E_g}{2q} + \frac{kT}{2q}\ln\left[\frac{N_c(1+3.75\alpha)}{N_v}\right] + \Delta E_g - \Delta E_v, \qquad (14)$$

where ΔE_g is the bandgap difference and ΔE_v is the band-offset of the valence band [15].

2.2. Generation-recombination models

Shockley-Read-Hall (SRH), Auger, radiative recombination, tunnelling, and optical generation are considered as the generation-recombination mechanism for HgCdTe. The SRH, Auger, and radiative models proposed by Rogalski [16,17] are implemented in the simulator. Tunnelling can be classified into two types in general, the indirect tunnelling via the trap level and direct tunnelling from the conduction band to the valence band or vice versa. The former one will be presented. The optical generation rate at a position is calculated by using ray trace method, which will be also presented.

2.2.1. Tunnelling models

Several analytic models for the indirect tunnelling have been proposed [5,19]. They took into account only pure tunnelling (PT) process based on the Sah model [20]. Recently, H. Yuan et al. [6] incorporated the phonon-assisted tunnelling (PAT) model in analysing the HgCdTe devices, which is originally intended to explain the tunnelling current of Si diode. The PT process is dominant at relatively high electric field and the PAT at low electric field. The PAT process consists of two successive procedures as shown in Fig. 2. An electron captured at the trap is emitted into a virtual level P located in the forbidden band by absorbing phonon energy, and then it transits into P′ by tunnelling without loss of time. In this work, two indirect tunnelling mechanisms are considered with a simple manner by extending the Hurkx model [21].

In the PAT process, the electron emission rate e_{PAT} can be calculated by multiplying ionisation energy reduction due to phonon by the tunnelling probability and integrating them along the depth of a potential well ΔE_n. In the PT process, e_{PT} is calculated by the modified Sah model [18,22]

$$e_{PAT} = e_{no}\int_0^{\Delta E_n/kT} \exp\left[z - z^{3/2}\,\frac{4(2m_e^*)^{1/2}kT^{3/2}}{3\hbar F}\right]dz, \qquad (15)$$

$$e_{PT} = \frac{\pi^2 q F m_e^* |M_e|^2}{\hbar^3 (E_c - E_T)}\exp(-2\theta_c), \qquad (16)$$

where m_e^* is the effective mass of the electrons, F denotes the electric field, M_c is the transition matrix element, θ_c is related to the electron wave function component directed to the tunnelling, z is the direction of the tunnelling and e_{no} is the emission rate when the electric field is zero.

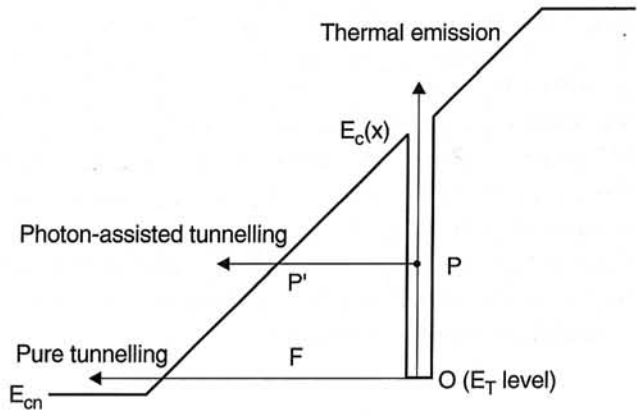

Fig. 2. Electron indirect tunnelling.

The integral interval, ΔE_n, varies with the trap location and level, $E_T(x)$ [18,21]

$$\begin{aligned} \Delta E_n(x) &= E_c(x) - E_T \quad \text{for } E_T > E_{cn}, \\ &= E_c(x) - E_{cn} \quad \text{for } E_T > E_{cn}. \end{aligned} \tag{17}$$

Total electron emission rate, then, can be expressed by

$$e_n = e_{no} + e_{PT} = e_{no}(1 + \Gamma_n^{PAT} + \Gamma_n^{PT}), \tag{18}$$

where Γ_n^{PAT} and Γ_n^{PT} are the normalised thermal emission rates. The same method is used for the hole. Following the work of Hurkx with the principle of the detailed balance, the generation-recombination rates regarding the tunnelling is obtained, which is in the form of the SRH generation-recombination rate

$$R_{trap} = \frac{pn - n_1 p_1}{\dfrac{\tau_{po}(n+n_1)}{1+\Gamma_p^{PAT}+\Gamma_p^{PT}} + \dfrac{\tau_{no}(p+p_1)}{1+\Gamma_n^{PAT}+\Gamma_n^{PT}}} \tag{19}$$

where τ_{n0} and τ_{p0} are the electron and hole intrinsic lifetime, respectively, and n_1 and p_1 are the electron and hole concentration as the Fermi level is located at the trap level. Further work is needed in calculating current with Eq. (19). Without the treatments it leads to a great amount of error in calculating the generation-recombination current. At first ($pn-n_1p_1$) should be zero at zero-bias in the dark state, which implies that no current flows at equilibrium. For the degeneracy the Fermi-Dirac statistics must be used in calculating n_1 and p_1. In practical, the form of n_{ie}^2 is better than that of n_1p_1. The term of n_1p_1 appeared in the Auger and radiative recombination rate is substituted by n_{ie}^2. Secondly, E_{cn} in equation (17) should be replaced by E_{fn} in the case of the degeneration. In addition the location of the trap level is testified to permit PT process. Since the tunnelling is available when there is an allowed state, E_{fn}, E_{fp}, E_c, E_v, and E_{cn} are compared each other along the direction of electric field at each position. The testing is also performed for the direct tunnelling [23]. A criterion of the direct tunnelling is given by as follows

$$E_v(E) \geq E_{cn} + MAX[0,(E_{fn} - E_{cn})]. \tag{20}$$

2.2.2. Optical generation model

When the radiation flux $Q_B(\lambda)$ emitted from the object with a constant temperature T_B is imposed on the devices, the carrier generation rate is given by

$$G_{opt}(y) = \int_0^{\lambda_{co}} [1 - R(\lambda)] Q_B(\lambda)\alpha(\lambda) \exp[-\alpha(\lambda)y] \sin^2\left(\frac{\theta_o}{2}\right) d\lambda \tag{21}$$

where λ_{co} is the cutoff wavelength, θ_0 is the field-of-view, $R(\lambda)$ is the reflectance [24,25], α is the absorption coefficient [26], and y is the distance from the incident surface. The $R(\lambda)$ and α are the function of the band gap or mole fraction. The band gap appeared in absorption coefficient should be replaced by the optical gap. The optical gap becomes E_{fn}–E_v for the degenerate case while it equals band gap energy for nondegenerate case, by which the Burstein-Moss shift [2] effect can be incorporated easily.

When the parameters have different values according to the position, especially for the heterostructure devices as in our case, the generation rate varies as well. We employ the ray-trace algorithm that can show the attenuation profile of incident flux with mole fraction and transmittance at each interface easily. Figure 3 shows the schematic representation of the algorithm. When the ray is incident to 3-layered material interfaced at the y_0, y_1, y_2 and y_3, the transmittances and fluxes are calculated at those interfaces. Because the last layer has can not absorb the ray stream, the flux is not changed. With the transmittances and fluxes, the generation rate is given by

$$G_{opt}(y) = \int_0^{\lambda_{co1}} T_0\, Q_B(\lambda)\alpha_1(\lambda)\exp[-\alpha_1(\lambda)(y - y_o)] \sin^2\left(\frac{\theta_o}{2}\right) d\lambda \quad \text{for } y_0 \leq y < y_1, \tag{22}$$

$$G_{opt}(y) = \int_0^{\lambda_{co2}} T_1\, Q_{B1}(\lambda)\alpha_2(\lambda)\exp[-\alpha_2(\lambda)(y - y_1)] \sin^2\left(\frac{\theta_o}{2}\right) d\lambda \quad \text{for } y_1 \leq y < y_2, \tag{23}$$

$$G_{opt}(y) = \int_0^{\lambda_{co3}} T_2\, Q_{B2}(\lambda)\alpha_3(\lambda)\exp[-\alpha_3(\lambda)(y - y_2)] \sin^2\left(\frac{\theta_o}{2}\right) d\lambda \quad \text{for } y_2 \leq y < y_3. \tag{24}$$

As the ray-trace method gives the transmission coefficient at each surface, it can consider the interfer-

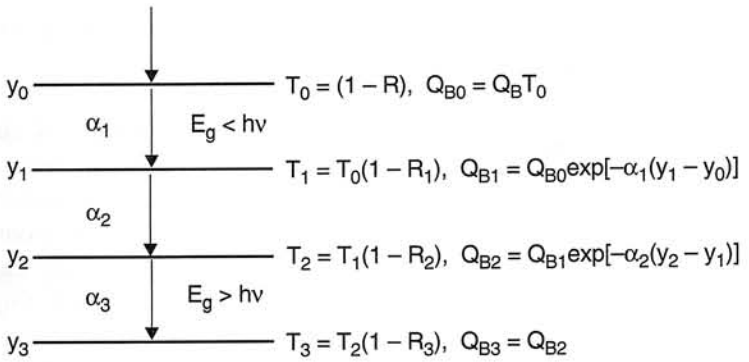

Fig. 3. Schematic representation of ray-trace algorithm.

ence by multiple reflections. It is, then, able to design the thickness of the layer and select the material to make an antireflection layer.

3. Numerical method

The solution of the basic semiconductor equations provides the internal distributions of carrier and electrostatic potential. The equations, however, cannot be solved analytically without the approximations even for the one-dimensional case. Therefore, the numerical method has to be applied. In general the method is composed of three steps, i.e., grid generation step, discretisation step transforming the differential equations into the linear equations, and solving step. The grid generation is a procedure of dividing the simulation area into a small segment called mesh and distributing the discretised points called node over the entire device region. It should not depend on the device structure. The small-generated node number is required in the view of the simulation time and memory capacity, but it should be enough that provide exact solutions. HYSEDES employs the triangular mesh type to be structure-free, and it has a grid generator developed using the qued-tree [27] and adaptive algorithms [28,29] for effective grid generation. It makes the simulator utilise in analysing the non-planar structures like the mesa structure or SPRITE detector structure [29]. The box integral method [30] is used in discretising the Poisson equation and current continuity equations, which is developed from the Gauss's law. It is a widely used method because of its simple discretisation procedure and its explicit guarantee of the carrier conservation in the discretisation procedure. After assembling the discretised equation, the matrix equation is formulated. Generally, the resulting matrix is sparse matrix. In solving the matrix equation, some treatment is required in assign non-zero element of the matrix to saving the memory [30]. The incomplete LU conjugate gradient squared (ILUCGS) method was used for solving the matrix instead of the direct Newton method. ILUCGS has been widely used for the reason that it can be applied to non-symmetric matrices and has high convergence speed and a few iterations [7].

4. Results and discussion

4.1. Photovoltaic devices

Though, theoretically, the zero-bias current should be zero in the dark state, many simulators provide non-zero current because of inherent errors in numerical techniques and improper modelling. If the current is overestimated when the optical signal imposed on the device, the signal source cannot be detected. The performance estimation in the dark state, then, becomes meaningless. The zero-bias current can be one of the indicator of good simulator for the devices such as HgCdTe photodiode.

Figure 4 shows the zero-bias currents calculated by HYSEDES in the dark state comparing with those obtained by MEDICI simulation. It is assumed that the mole fraction x of $Hg_{1-x}Cd_xTe$ is 0.2, the doping concentrations of p–type and n–type HgCdTe are 5×10^{15} cm^{-3} and 5×10^{17} cm^{-3}, respectively; the lifetime of the carriers is 50 ns, the surface recombination velocity is 2×10^4 cm/s, and the fixed charge density at the interface is 8×10^{10} cm^{-2}. It is also assumed the impurity being completely ionised regardless of the mole fraction and temperature. As the mole fraction is lower and the temperature is higher, the currents calculated from MEDICI, which is well-known commercial device simulator, show higher values. It is because of the effect of nonparabolic band and degeneracy. At the low mole fraction the energy gap is small and the nonparabolic factor is large. The band, then, becomes highly degenerated. As temperature in-

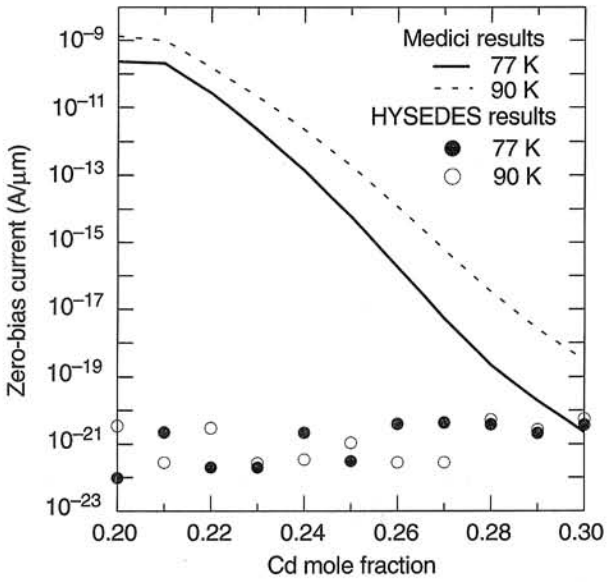

Fig. 4. Zero-bias dark current in HgCdTe photovoltaic device.

creases, the effect of the nonparabolicity and the degeneracy are weakened. However, since the intrinsic carrier concentration at 90 K is higher than that at 77 K, the values of $(pn - n_i^2)$ could be higher at 90 K showing the higher zero-bias current. These results demonstrate that conventional simulators have problems not only in the low temperature region but also in the high temperature region. As shown in Fig. 4, the extremely low zero-bias dark current by the HYSEDES simulation proves its validity.

Figure 5 represents the temperature dependency on R_0A. The parameters used in this simulation are same as that given by the experiment [31]. Because the trap-related parameters are not given, it is assumed that the trap density is 1.0×10^{13} cm^{-3}, the trap energy is $0.6E_g$. Simulations are performed with the carrier capture rate of 8.0×10^{-9} cm^{3}s^{-1} labelled 1 in the figure and of 8.0×10^{-8} cm^{3}s^{-1} labelled 2. The curve 1 accorded with the experimental data shows the diffusion-limited characteristics at above 50 K and indirect tunnelling-limited characteristics with gentle slope at below 50 K. The curve 2 with 10 times larger capture rate than curve 1 shows the SRH-limited characteristics from 77 K to 55 K. The more gentle slope of the line from 45 K to 55 K than that of the SRH-limited case is due to the effect of phonon-assisted tunnelling. The temperature, from which the indirect tunnelling dominant region begins, shows the identical value of about 45 K regardless of the capture rate. It can be explained by the fact that the indirect tunnelling dominant region is determined mainly by the distribution of electric field at the junction while the value of the dark-current and R_0A are controlled by the trap-related parameters.

Figure 6 shows the electrical characteristics of HgCdTe device in the dark state, the bias dependency on current and dynamic resistance R_DA for the homojunction structure, heterojunction structure, and heterojunction structure with potential barrier at the junction, respectively. All the calculating conditions are the same as those used in Fig. 5 except the trap density of 1.0×10^{14} cm^{-3} and the capture rate of 2.0×10^{-8} cm^{3}s^{-1}. In Fig. 6 (a), R_DA is in almost constant value from 0 to –60 mV for the case of the homojunction and to –100 mV for the heterojunction without barrier. It implies that not only SRH but also the indirect tunnelling mechanisms have an influence on the current in those regions, since when only SRH is the primary mechanism in current formulation R_DA would increase in proportion to the square of the bias voltage. As the bias increases resulting in high electric field and large band overlap, R_DA decreases rapidly because of increased leakage current by the indirect tunnelling and the band-to-band direct tunnelling. The difference in the value of R_DA is about 2.35 times, and it grows to about one order at the region where the indirect tunnelling is dominant. The breakdown voltage caused by the direct tunnelling for the case of the heterojunction without barrier is increased about 60 mV with respect to that for the homojunction. This value is almost equal to half of the bandgap difference between the materials used as a capping layer and the absorption layer. The improved performances in the

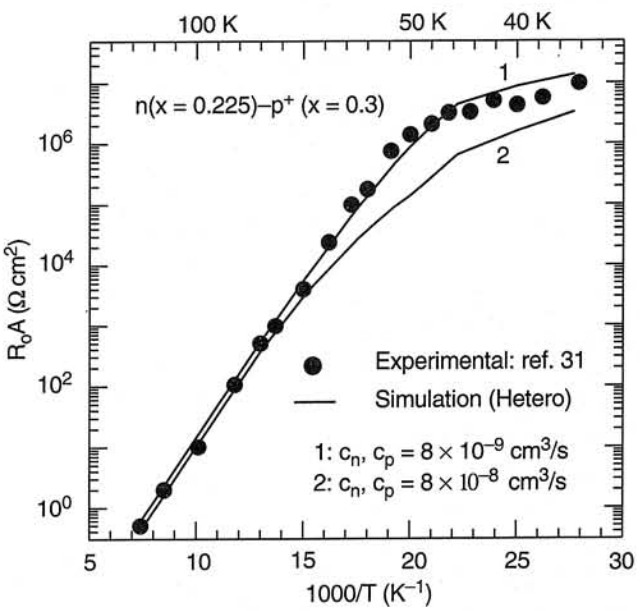

Fig. 5. R_0A dependence on the temperature of a HgCdTe heterostructure photovoltaic device.

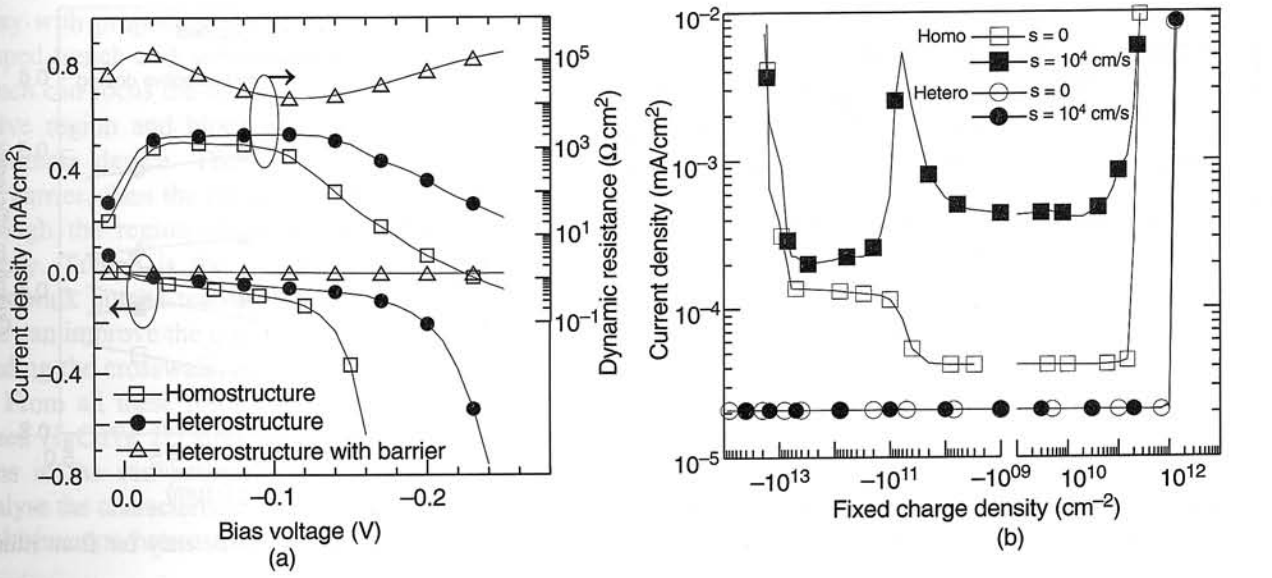

Fig. 6. Current and dynamic resistance with applied bias for homojunction and heterojunction structures with and without barrier (a), leakage current density as a function of fixed charge density (b).

heterojunction is originated from the higher tunnelling barrier and lower intrinsic carrier concentration accomplished by the high mole fraction of the capping layer. In the heterojunction with barriers, the p–n junction is formulated in the wide bandgap p–layer, where the potential barrier is built up in the valence band. The little current, then, flows at dark state because the potential barrier limits hole injection to the p–type region. It means that the excess carriers generated optically can not move through the barrier, which leads to relatively low detectivity.

Figure 6 (b) shows the leakage currents as a function of fixed charge density at the interface between HgCdTe active layer and CdTe surface protection layer for the homostructure and heterostructure photovoltaic devices. With the supply voltage of –20 mV two surface recombination velocities of zero and 10^4 cms^{-1} are used. As the positive fixed charge increases, more electrons are accumulated at the interface resulting in narrow depletion width. The SRH generation-recombination current, then, decreases while the indirect tunnelling current increases. The various aspects of the current are obtained according to the primary mechanism except at high fixed charge density where the direct tunnelling process dominates. When the surface is depleted by negative charges, thermal generation-recombination has a primary role on the current. Thus the current increases slowly with the charge density. Much higher charge density induces the direct tunnelling leading high current. For the homojunction with the surface recombination velocity 10^4 cms^{-1}, the current increases slowly to the values of -6×10^{10} cm^{-2} in fixed charge density and then decreases to show peak. It is attributed to the degradation of carrier generation at the surface by the surface recombination velocity. The similar result has been presented in Rosbeck's experiment [32]. The heterostructure shows an excellent leakage current characteristics regardless of the high surface recombination velocity. As a result, it is confirmed that heterojunction structure is useful in controlling the generation of leakage current because of its low tunnelling probability and a low minority carrier concentration at the surface.

4.2. Crosstalk in focal plane array

To get the high quality thermal image, the integration of focal plane array (FPA) is in increasing. The size of a device shrinks to the diffusion length of the minority carrier or absorption length. The crosstalk becomes, then, an issue. The crosstalk is the phenomenon that the photo-generated carriers in a device active region are detected not only at the device but also at the proximate device by lateral diffusion. Generally, the crosstalk is in trade-off relation with quantum efficiency. When the crosstalk is reduced, the quantum efficiency is also degraded. Most probable way of suppressing crosstalk is the isolation of the element devices. This is accomplished by physically as trench or by electrically as junctions. Trench is most reliable way but its realisation is obscure. The junction such as p–n junction called guard ring is more realistic but it wastes the total device size. There is a

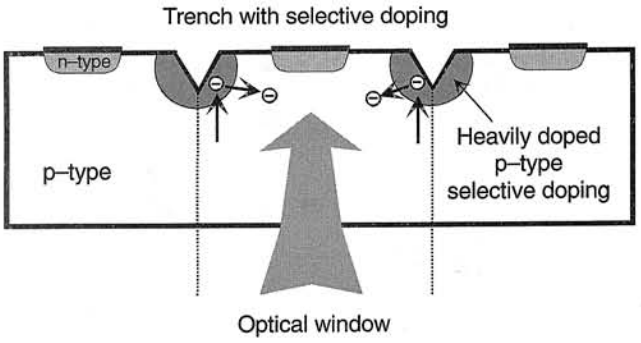

Fig. 7. Proposed structure with trench and selective doping.

common contact in the isolation area. Therefore, although the isolation can block the diffusion path, the carriers reached isolation region are swept out through the common contact resulting loss in quantum efficiency.

We propose a structure with triangle shaped trench and selective doping, as shown in Fig. 7, to reduce crosstalk without degrading quantum efficiency. The mole fraction is 0.3, temperature 77 K, p-sub density 5×10^{15} cm^{-3}, selective doping density 1×10^{17} cm^{-3}. The conceptional idea is that the triangle shaped trench has role on crosstalk and bulk-like type heavily doped region formulates a barrier blocking minor carrier diffusion. Triangle shape with common contact reflects the light to the centre of the device active region, which also enhances the quantum efficiency. The characteristics are compared with two other structures, one with common contact and the other with triangle shaped trench. Under the back illumination, the quantum efficiency of the proposed structure is not degraded while that

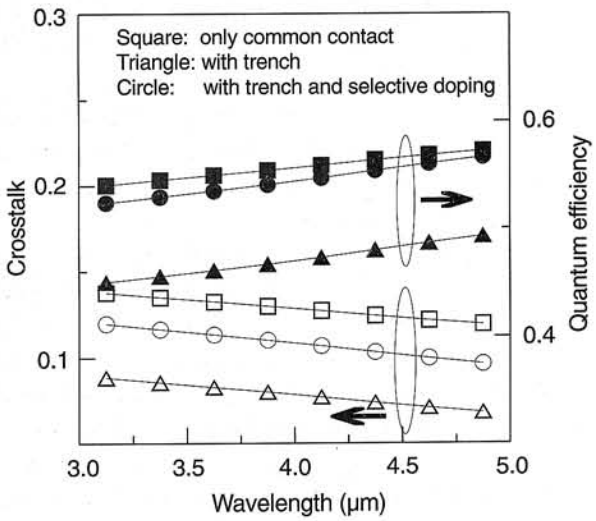

Fig. 8. Crosstalk and quantum efficiency for back illumination.

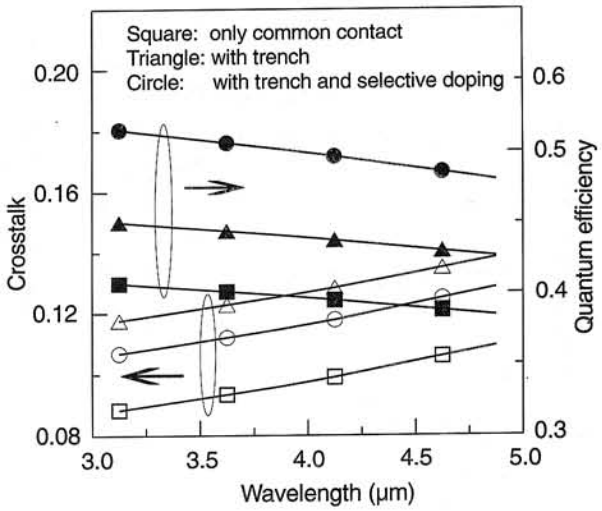

Fig. 9. Crosstalk and quantum efficiency for front illumination.

of triangle shaped trench is largely reduced. As expected, the crosstalk of proposed structure increases but not over 12%, as shown in Fig. 8. For front illumination case, as shown in Fig. 9, the quantum efficiency of proposed structure greatly improved because the photo generated carriers near the device surface can not diffuse by the barrier.

5. Conclusions

We present a HgCdTe 2D simulator having the capability of calculating accurately the characteristics of the HgCdTe devices. The improper consideration of the conduction band nonparabolicity and the degeneracy in the calculation of the carrier concentration causes higher zero-bias current. By including those inherent material characteristics of HgCdTe into the carrier transport equations and the generation-recombination models, the zero-bias current in the dark state is in the very low level. Furthermore, various generation-recombination models including the indirect tunnelling mechanism are implemented in this simulator to investigate the source of the leakage current in the dark state. Those allow good agreement with the experimental data even at the low temperature region where the tunnelling has great role in the current.

Simulations for some photovoltaic devices and focal plane array demonstrate the broad application capability of the proposed simulator giving their several important characteristics. As for the photovoltaic devices, the performance improvements in the heterostructure were evaluated by comparing those in the homojunction structure and two heterojunction structures. We also present the crosstalk in the focal plane

array with proposing the new structure with triangle shaped trench and selective doping. Triangle-shaped trench can focus the incident light to the centre of the active region and block the carrier diffusion to the proximate device. The selective doping formulates the barrier, then the minor carrier can diffuse hardly through the region resulting in high quantum efficiency. Trench is the promising way for reducing crosswalk but its realisation is uncertain. The structure can improve the quantum efficiency with low degrading the crosswalk.

From all these results, we conclude that the proposed HgCdTe 2D simulator can resolve some problems in the conventional simulators completely and analyse the characteristics of various devices including multi-junction heterostructure and focal plane aray.

References

1. K. Kosai, "Status and application of HgCdTe device modelling", *J. Electr. Mater.* **24**, 635–640 (1995).
2. D.H. Mao, H.G. Robinson, D.U. Bartholomew, and C.R. Helms, "Device modelling of HgCdTe vertically integrated photodiodes", *J. Electr. Mater.* **26**, 678–682 (1995).
3. G.M. Williams and R.E. DeWames, "Numerical simulation of HgCdTe detector characteristics", *J. Electr. Mate.* **24**, 1239–1248 (1995).
4. V. Ariel, "Modelling of heterojunction HgCdTe photodiodes using **kp** approach", *J. Electr. Mater.* **26**, 673–677 (1997).
5. D. Rosenfiled and G. Bahir, " A model for trap-assisted tunnelling mechanism in diffusion n-p and implanted n^+-p HgCdTe photodiodes", *IEEE Tran. Electron Devices* **39**, 1638–1645 (1992).
6. H. Yuan, F. Tong, and D. Tang, "Contribution of field enhanced generation-recombination to $Hg_{1-x}Cd_xTe$ photodiode characteristics", *Infrared Phys.* **31**, 451–458 (1991)..
7. *MEDICI Manual*, Technology Modelling Associates Inc., 1994.
8. S. Selberherr, *Analysis and Simulation of Semiconductor Devices*, Springer-Verlag, Wien, 1984.
9. W.H. Press, S.A. Teukolsky, W.T. Vettering, and P. Flannery, *Numerical Recipes in C*, Cambridge Univ. Press, London, 1991.
10. H. Barry and C.R. Ratliff, "Numerical tabulation of integral of fermi functions using **k.p** density of states", *J. Appl. Phys.* **42**, 3189–3194 (1971).
11. D. Chattopadhyay and B.R. Nag, "Scattering mechanisms in $Hg_{1-x}Cd_xTe$", *Phys. Rev.* **B12**, 5676–5681 (1975).
12. Z. Yu and R.W. Dutton, *SEDAN III-A Generalised Electronic Material Device Analysis Program*, Technical Report, Stanford University, 1985.
13. C.C. Matthai and R.H. Williams, in *Physics and Techonology of Heterojuntion Devices*, edited by P. Peregrinus, 1991.
14. P. Migliorate and A.M. White, "Common anion heterojunctions: CdTe-CdHgTe", *Solid State Elctronics* **26**, 65–69 (1983).
15. E.A Kraut, "The effect of a valance-band offset on potential and current distributions in HgCdTe heterostructures", *J. Vac. Sci. Technol.* **A7**, 420–423 (1989).
16. A. Rogalski and R. Ciupa, "Long-wavelength HgCdTe photodiodes: n^+-on-p versus p-on-n structures", *J. Appl. Phys.* **77**, 3505–3512 (1995).
17. A. Rogalski, A. Jóźwikowski, and J. Rutkowski, "Performance of p^+-n HgCdTe photodiodes", *Infrared Phys.* **30**, 463–473 (1992).
18. W.W. Anderson and H.J. Hoffman, "Field ionisation of deep levels in semiconductors with applications to HgCdTe p-n junction", *J. Appl. Phys.* **53**, 9130–9145 (1982).
19. Y. Nemirovsky, R. Fastaw, M. Meyassed, and A. Unikovsy, "Trapping effects in HgCdTe", *J. Vac. Sci. Technol.* **B9**, 1829–1839 (1991).
20. C.T. Sah, "Electronic processes and excess currents in gold-doped narrow silicon junctions", *Phys. Rev.* **123**, 1594–1621 (1961).
21. G.A. Gurkx, D.B. Klassen, and M.P. G. Knuvers, "A new recombination model for device simulation including tunnelling", *IEEE Trans. Electron Devices* **39**, 331–338 (1992).
22. G. Vincent, A. Chantre, and D. Bois, "Electric field effect on the thermal emission of traps in semiconductor junctions", *J. Appl. Phys.* **50**, 5484–5487 (1979).
23. P.K. Chakraborty and J.C. Biawas, "Theory of interband tunnelling in semiconductor", *Solid State Electronics* **28**, 493–497 (1985).
24. S.E. Schacham and E. Finkman, "Recombination mechanisms in p-type HgCdTe; Freezeout and background flux effects", *J. Appl. Phys.* **57**, 2001–2009 (1985).
25. E. Finkman and S.E. Schacham, "The exponential optical absorption band tail of $Hg_{1-x}Cd_xTe$", *J. Appl. Phys.* **56**, 2896–2900 (1984).

26. C.A. Hougen, "Model for infrared absorption and transformation of liquid phase epitaxy HgCdTe", *J. Appl. Phys.* **66**, 3763–3766 (1989).
27. S.H. Lo, "A new mesh generation scheme for arbitrary planar domains", *Int. J. Numerical Method in Eng.* **21**, 1403–1426 (1985).
28. W.M. Coughran, M.R. Pinto, and R.K. Smith, "Adaptive grid generation for VLSI device simulation", *IEEE Trans. Electron Devices* **10**, 2359–2375 (1991).
29. C.T. Elliot, D. Day, and B.J. Willson, "An integrating detector for serial scan thermal imaging", *Infrared Phys.* **22**, 31–42 (1982).
30. M.R. Pinto, *Comprehensive Semiconductor Device Simulation for Silicon ULSI*, PhD. Thesis, Stanford Univ., 1990.
31. J.M. Arias, J.G. Pasko, M. Zandian, S.H. Shin, G.M. Williams, and L.O. Bubulac, "Planar p-on-n HgCdTe heterostructure photovoltaic detectors", *Appl. Phys, Lett.* **52**, 976–978 (1993).
32. J.P. Rosbeck and E.R. Blazejewski, "Investigation of generation process at the SiO_2/HgCdTe interface by gate controlled diodes", *J. Vac. Sci. Technol.* **A3**, 280–284 (1985).

